APPLIED SCIENCES AND ENGINEERING

3D steerable, acoustically powered microswimmers for single-particle manipulation

Liqiang Ren[1], Nitesh Nama[2], Jeffrey M. McNeill[3], Fernando Soto[4], Zhifei Yan[1], Wu Liu[1], Wei Wang[5]*, Joseph Wang[4]*, Thomas E. Mallouk[1,3]*

The ability to precisely maneuver micro/nano objects in fluids in a contactless, biocompatible manner can enable innovative technologies and may have far-reaching impact in fields such as biology, chemical engineering, and nanotechnology. Here, we report a design for acoustically powered bubble-based microswimmers that are capable of autonomous motion in three dimensions and selectively transporting individual synthetic colloids and mammalian cells in a crowded group without labeling, surface modification, or effect on nearby objects. In contrast to previously reported microswimmers, their motion does not require operation at acoustic pressure nodes, enabling propulsion at low power and far from an ultrasonic transducer. In a megahertz acoustic field, the microswimmers are subject to two predominant forces: the secondary Bjerknes force and a locally generated acoustic streaming propulsive force. The combination of these two forces enables the microswimmers to independently swim on three dimensional boundaries or in free space under magnetical steering.

INTRODUCTION

The ability to precisely transport and position micro/nanomaterials at the single-particle level plays an essential role in advancing science and clinical applications, such as nano/micro synthesis, cell transcriptomics and mechanics, biomanufacturing, and drug delivery (*1*–*3*). Over the past few decades, many techniques for particle manipulation have been developed to meet this demand. Traditional methods use microneedles or micropipettes controlled by mechanical stages to physically contact their targets (*4*). Although these direct contact techniques can target individual particles and provide strong interactions, the needles/pipettes are fragile, expensive, vulnerable to contamination, and can operate only in open environments. In contrast, contactless tweezing techniques trap particles by means of an externally supplied field gradient, such as an optical, electrical, or acoustic field. Trapped particles are then manipulated by dynamically changing the field. So far, optical tweezers have been the most widely adopted contactless technique for single-particle manipulation (*5*). Focusing light to small dimensions enables optical tweezers to trap individual cells, bacteria, or virus particles and move them in three dimensions (3D). However, high-intensity light has been reported to cause damage in some biological applications. Compared to optical tweezers, acoustic and magnetic tweezers have obvious advantages in terms of biocompatibility and penetration depth (*6*, *7*). However, neither method has so far been capable of independently manipulating individual particles in a dense environment due to the difficulty in shaping and focusing acoustic and magnetic fields.

Recently, the development of microswimmers has provided a promising alternative for single-particle manipulation. Microswimmers powered by chemical reactions or external fields are able to move independently of each other and of passive particles (*8*, *9*). They can move among particles, pick up individual ones, and transport them without affecting others (*10*–*12*). So far, the most sophisticated particle manipulations, such as single-particle, label-free loading, and 3D transport, have been demonstrated with magnetically propelled microswimmers (*13*–*15*). These microswimmers rotate in dynamic magnetic fields and move based on the rotation-induced viscous force. However, the rotation causes fluidic streaming around the microswimmers and can undermine the precision of particle manipulation.

As another biocompatible energy source, acoustic fields can propel microswimmers at faster speeds than magnetic swimmers and can be actuated in simpler devices (*16*, *17*). To date, acoustic microswimmers based on various mechanisms, including standing acoustic wave streaming–propelled metallic microrods (*18*), vibrating flagella (*19*, *20*), and oscillating bubbles (*21*–*26*), have been developed. Despite their behavior, none of these microswimmers has demonstrated satisfactory tweezing or micromanipulation capability. Metallic microrods, which are simple to fabricate by template electrodeposition in batches of ~10^8 particles, can load, transport, and release cargo on demand upon actuation by acoustic or magnetic fields (*27*–*29*). However, both the microrods themselves and their targets are confined to standing wave pressure nodes during operation, a limitation common to conventional acoustic tweezers. The vibrating flagella and oscillating bubble motors can work in arbitrary traveling acoustic waves and avoid the potential trapping force at acoustic pressure nodes. However, high acoustic power is needed to vibrate the soft flagella. The high power can cause undesirable bulk streaming and damage to biological samples. Furthermore, these swimmers are large (millimeters to hundreds of microns) and difficult to steer because of the limitations of their fabrication methods. Neither the flagella nor the bubble-based swimmers have been used to demonstrate particle manipulation. Recently, the Marmottant Group (*30*) has applied direct laser writing techniques to fabricate bubble-based swimmers on the tens of microns scale. Their design allowed the swimmers to hover over a substrate and achieve very high speeds (17,500 body lengths/s speed at 24-kPa acoustic pressure). (*31*). Although sophisticated motion control has not been demonstrated, this work points out a possible direction for addressing the remaining challenges.

Here, we present a design for acoustically powered bubble-based microswimmers that can selectively manipulate individual particles and mammalian cells in a crowded environment without labeling, surface modification, or effect on nearby objects. Unique behaviors

[1]Department of Chemistry, Biochemistry and Molecular Biology, Physics, and Engineering Science and Mechanics, Pennsylvania State University, University Park, PA 16802, USA. [2]Department of Surgery, University of Michigan, Ann Arbor, MI 48109, USA. [3]Department of Chemistry, University of Pennsylvania, Philadelphia, PA, 19104, USA. [4]Department of Nanoengineering, University of California San Diego, La Jolla, CA 92093, USA. [5]School of Materials Science and Engineering, Harbin Institute of Technology (Shenzhen), Shenzhen, Guangdong 518055, China.
*Corresponding author. Email: weiwangsz@hit.edu.cn (W.W.); josephwang@ucsd.edu (J.W.); tem5@psu.edu (T.E.M.)

of these microswimmers include self-alignment at boundaries, magnetic speed regulation, climbing of boundary walls, and autonomous or field-directed swimming in 3D. When excited by an acoustic wave at the resonant frequency of the bubble, the microswimmers immediately align themselves normal to a nearby boundary and statically hover on it. By simultaneously applying an external magnetic field, one can change the orientation of the microswimmers and initiate their translational motion. Not only the direction of the motion but also the speed can be precisely regulated by the direction of the external magnetic field. At an acoustic pressure level (~4 kPa) that does not generate obvious acoustic bulk streaming or trapping forces on passive particles, the microswimmers can be propelled at a remarkable high speed of 2.6 mm/s (350 body lengths/s). The strong propulsive force and precise directional control enable the microswimmers to pick up individual passive particles and relocate them to arbitrary positions in a highly dense sample. Moreover, the microswimmers can climb vertical boundaries or swim in free space, which allows them to operate robustly and reliably in complex environments. Combined with the contactless, biocompatible nature of their propulsion, this versatile microswimmer platform could serve as a powerful tool in advanced biomedical research and clinical therapy.

RESULTS

The microswimmers have a half-capsule shape that is fabricated through a combination of high-resolution direct laser writing and metallic layer deposition, as illustrated in fig. S1. Briefly, the half-capsule structure that serves as the main body of the microswimmer was printed on a silica substrate by a 3D direct laser lithography technique with polymer photoresist IP-Dip. The capsule was designed to have a shell thickness, outer diameter, and length of 500 nm, 5 μm, and 7.5 μm, respectively (Fig. 1A). Then, a thin magnetic nickel layer (10 nm) was deposited onto the capsule by directional electron beam deposition, followed by sputter deposition of a uniform gold layer (40 nm). After the metallic layers were deposited, the surface was modified to be hydrophobic by heating the sample in trichlorosilane vapor at 70°C for 15 min. Last, the capsules were scratched off the substrate and transferred to an acoustofluidic chamber (Fig. 1B) for characterization. When submerged in the fluid, an air bubble was spontaneously trapped in each capsule to form the microswimmers. The hydrophobic treatment is a crucial step for successfully trapping air bubbles. The optional Au layer deposition was used to control the buoyancy of the microswimmers so that they could sink to the bottom of the fluidic chamber. Without the Au layer, the microswimmers floated on the top of the fluid (Fig. 1B), and the air bubble-water interface could be observed (fig. S2). Microswimmers fabricated in this fashion can operate continuously for several hours with only a slight change in the working frequency. No bubble expulsion or dissolution was observed in 2 hours during our experiments. The acoustofluidic chamber was composed of a polymer spacer, a silicon wafer, and a microscope glass coverslip, and the acoustic field was generated by a piezoelectric ceramic transducer that was attached to the bottom of the silicon wafer. An external magnetic field was provided by manually holding a cylindrical magnet next to the chamber. During the experiments, the sample cell was placed on the stage of an upright microscope, and the behavior of the microswimmers was observed from the top through the glass coverslip. Additional details can be found in Materials and Methods.

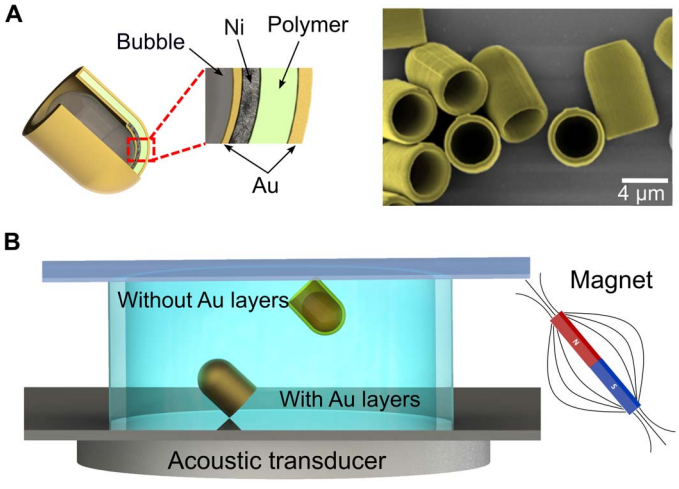

Fig. 1. Schematic of the microswimmers and the acoustofluidic chamber. (**A**) Schematic and false-colored scanning electron microscopy image of microswimmers (with Au layers). (**B**) Schematic of the acoustofluidic chamber. The microswimmers with and without the Au layer sink to the bottom or float to the top of the chamber, respectively.

Propulsion mechanism

When a microswimmer is exposed to an acoustic field, the gas bubble encapsulated in the microswimmer pulsates, creating three distinct forces: (i) a primary Bjerknes force F_{PB}, (ii) a streaming propulsive force F_{SP}, and (iii) a secondary Bjerknes force F_{SB}, as shown in Fig. 2A. The primary Bjerknes force originates from scattering of the imposed background acoustic waves by the oscillating bubble and has the same direction as the direction of wave propagation (*32*). However, the scale of the primary Bjerknes force is much smaller than the streaming propulsive force ($\frac{F_{SP}}{F_{PB}}$~10) and therefore can be neglected (*31*). The streaming propulsive force is generated by cavitation microstreaming, which is induced by the high-frequency oscillation of the water-air interface. Because of the asymmetric configuration of the microswimmer, a net cavitation microstream flows away from its open end. The net streaming results in a propulsive force F_{SP} that is in the opposite direction of the streaming from the microswimmer, which is thus propelled along its long axis. F_{SP} scales as $F_{SP}\sim\varepsilon^2\rho_f a^4 f^2$, where a is the radius of the bubble, εa is the amplitude of oscillation of the bubble, ρ_f is the density of the fluid, and f is the frequency (*30*). Last, because of the presence of a rigid boundary in its vicinity, the microswimmer experiences a secondary Bjerknes force F_{SB}. The presence of the boundary is equivalent to the presence of an image bubble that is positioned symmetrically to the real bubble with respect to the boundary (*33*). Since the image bubble always oscillates in phase with the real bubble, it exerts an attractive force on the real bubble and pulls the bubble toward the boundary. This force can be expressed as $F_{SB}\sim-\frac{\rho_f}{4\pi d^2}\langle\dot{V}\rangle^2$, where d is the distance between the centers of the real and image bubbles (i.e., twice the distance from the center of the bubble to the boundary), V is the volume of the bubble, $\langle\,\rangle$ denotes the time average, and the dot indicates the time rate of change. The ratio of the secondary Bjerknes force to the streaming propulsive force is $\frac{F_{SB}}{F_{SP}}\sim4\pi(a/d)^2$. Since the secondary Bjerknes force is always normal to the boundary, the motion of the microswimmer in the direction parallel to the boundary is determined by its orientation and axial streaming propulsive force. The motion in the perpendicular direction can be dominated either by the streaming propulsive force or by the secondary Bjerknes force, resulting in swimming away from

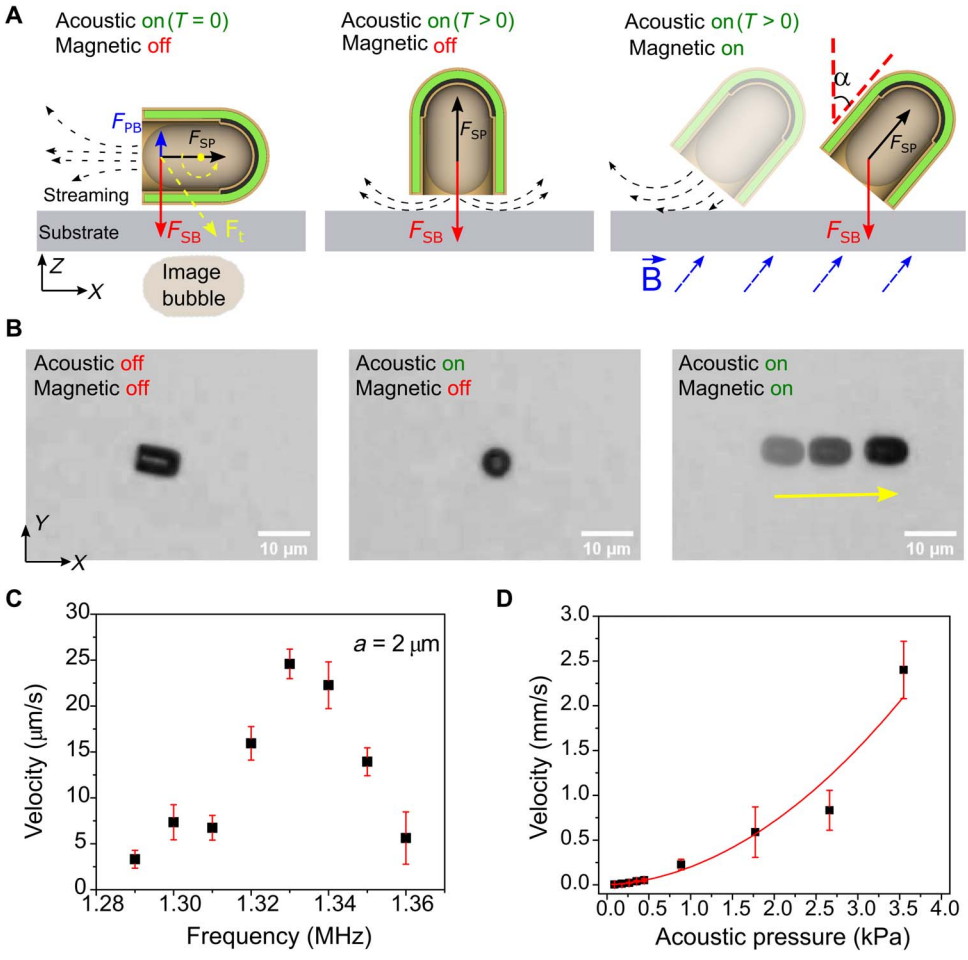

Fig. 2. Theoretical analysis and experimental demonstrations of the microswimmers' behaviors responding to an acoustic field and a magnetic field. (**A**) Schematic of the primary Bjerknes force F_{PB} (blue solid arrow), secondary Bjerknes force F_{SB} (red solid arrow), and streaming propulsive force F_{SP} (black solid arrow) on a microswimmer at the moment that an acoustic field is applied ($T = 0$). The yellow dot indicates the center of mass of the microswimmer, and black dashed arrows indicate the streaming flow pattern. The total force (yellow dashed arrow) generates a torque to rotate the axis of the microswimmer into the z direction. When the magnetic field is on (blue dashed arrows), the microswimmer is tilted at an angle α and starts to translate. (**B**) Experimental demonstrations (top view) of the self-rotation of microswimmers when the acoustic field is on and the translation of microswimmers over 2 s when both acoustic and magnetic fields are applied. (**C**) Dependence of the speed of the microswimmers upon the acoustic frequency in a constant magnetic field. (**D**) The relationship of the speed of microswimmers and applied acoustic pressure; the red line is a quadratic fit.

or attachment to the boundary. The relative strength of these forces depends on the distance between the center of the bubble and the boundary. These two forces together govern the behavior of the microswimmer and distinguish it from other acoustic bubble swimmer platforms.

In the absence of the acoustic field, the microswimmers rest at the bottom of the chamber with their long axis parallel to the substrate. Immediately upon applying the acoustic field, the two forces emerge to act on the microswimmers (Fig. 2A, $T = 0$). The position of action of the secondary Bjerknes force should be close to the open end, whereas the center of mass of the microswimmer is away from the water-air interface, considering the asymmetric design. As a result, the total force generates a torque that rotates the long axis of the microswimmers into the z direction. This torque disappears when the streaming propulsive force and secondary Bjerknes force align in the z direction ($T > 0$). In this orientation, the streaming propulsive force is cancelled by the secondary Bjerknes force, leading to a quiescent state of the microswimmers. The translational motion of the microswimmer can then be initiated upon applying an external magnetic field. The Ni layer on the microswimmers responds to the external magnetic field and rotates the microswimmers to an angle α, resulting in a net propulsive force $F_{SP} \cdot \sin(\alpha)$ in the x-y plane. The microswimmers then move in the direction of the net propulsive force.

Experimental demonstrations of the self-rotation and translation of microswimmers are shown in Fig. 2B. The microswimmer orients normal to the substrate with its open end (air-water interface) facing the bottom when the acoustic field is applied (movie S1). In this position, no translational motion of the microswimmer was observed. When a cylindrical magnet (pulling force, 200 N) was placed next to the fluidic chamber, the microswimmers started to translate in the direction of their closed ends. The direction of movement could be precisely steered by the direction of the magnetic field (movie S2). Control experiments demonstrated that the microswimmers stopped translating immediately when the acoustic field was turned off and that capsules without a trapped air bubble neither self-rotated nor translated in the same acoustic field. Therefore, both the self-rotation and the

translational motion of the microswimmers are powered by the acoustic field, while the magnetic field acts as a switch to initiate the translational motion by controlling the direction of the streaming propulsive force.

Acoustic frequency and power dependence

In a magnetic field with a fixed direction (α = 45°), the motion of the microswimmers is sensitive to the applied acoustic frequency. As shown in Fig. 2C, a microswimmer reached its fastest speed at a frequency of 1.33 MHz. In general, the streaming propulsive force reaches a maximum at the resonant frequency of the bubble. The resonant frequency of a bubble trapped inside a microswimmer can be estimated from Eqs. 1 and 2

$$f_0 = \frac{1}{2\pi}\left(\frac{\kappa P_0}{\rho(L - L_b)L_b}\right)^{1/2} \cdot M \quad (1)$$

$$M = \left(1 + \frac{4\gamma L_b}{\kappa P_0 a^2}\right)^{1/2} \quad (2)$$

where κ ~ 1.4 is the adiabatic index, ρ is the liquid density, P_0 is the undisturbed pressure in the bubble, L_b is the length of the bubble inside the microswimmer, L is the total tube length, a is the inner radius, and γ ~ 0.07 N/m is the surface tension of the water-air interface. M is a correction factor that considers the surface tension effect (details in the Supplementary Materials) (*34*).

In our experiment, the measured resonant frequency of the microswimmers (L = 7 μm and a = 2 μm) was distributed over a range of 1.1 to 1.4 MHz, as shown in fig. S3A. According to Eq. 1, the distribution of the resonant frequencies implies a distribution of bubble lengths L_b from 4.7 to 5.7 μm (fig. S3B). The distribution in bubble lengths L_b is reasonable considering the fabrication process. A peak in the distribution around 1.3 MHz indicates the potential to simultaneously propel collections of microswimmers at a single frequency. The equation for estimating the resonant frequency was also validated by characterizing a smaller microswimmer (L = 4 μm and a = 1 μm). A resonant frequency at 2.57 MHz was observed (fig. S4), corresponding to a bubble length L_b of 2.7 μm.

At the resonant frequency, the acoustic propulsion force is proportional to the square of applied acoustic pressure (Fig. 2D) (*30*). Speeds as fast as 2.6 mm/s (~350 body lengths/s) were observed at an acoustic pressure level of 4 kPa. Neither tracer particles nor microswimmers were trapped at acoustic pressure nodes nor was the generation of bulk acoustic streaming observed in the chamber. Although we conducted our experiments in a closed chamber, the microswimmers do not require standing acoustic waves for propulsion. The microswimmers behaved in a similar manner when we changed the height of the chamber (120, 180, and 240 μm). Without confinement by acoustic pressure patterns that are typically seen with microrod acoustic motors, the bubble-based microswimmers were able to travel millimeter distances in the chamber at high speeds.

Note that the overall density of the microswimmers was much smaller than that of the fluid (polymer to air volume ratio, ~1:1; polymer density, ~1.2 kg/m^3) when the Au layer was not included in fabrication. For this reason, the uncoated microswimmers always floated to the top surface of the fluidic chamber. Despite the difference in their location, they behaved in the same way as those on the bottom in the acoustic-magnetic field. Specifically, the floating microswimmers aligned themselves vertically at the top cover with the water-air interface facing up in the acoustic field and were similarly propelled when tilted by the magnetic field (fig. S5). Subtle changes in the propulsion speeds of the microswimmers were observed. These floating microswimmers may have some utility in applications at the air-water interface, such as particle assembly or separation of hydrophobic contaminants.

Magnetic regulation

Besides acoustic frequency and power, the translational speed of the microswimmers can also be regulated by the magnetic field. As shown in Fig. 3A, the same microswimmer traveled different distances during 2 s when it was tilted at different angles α (movie S3). α is determined by the direction of the magnetic field and measured by the orientation of the cylindrical magnet. At a constant acoustic pressure input (~300 Pa), the speed of the microswimmers increased as α increased and reached a peak value at about 60°. A significant decrease in speed was observed when α was increased to 90° (Fig. 3B).

The streaming generated by bubble oscillation was numerically simulated in COMSOL Multiphysics to provide a qualitative understanding of the mechanism by which α affects the speed. For simplicity, we introduced the acoustic field by assuming a radial oscillation of the water-air interface (red dashed line in Fig. 3C). As shown in Fig. 3C, when the microswimmer is aligned vertically to the boundary (α = 0°), the streaming is symmetrically distributed on both sides, and there is no propulsive force in the x direction. However, when the microswimmer is realigned by the magnetic field (α = 45°), the symmetry of the streaming is broken, resulting in a net x component of the streaming propulsive force. A larger tilt angle leads to a larger x component of the hydrodynamic stress and a larger propulsive force (Fig. 3B). Therefore, the external magnetic field regulates the speed of the microswimmer by steering the direction of the steaming propulsive force.

The simulation indicates that the translational velocity of the microswimmer should reach a peak velocity at α = 90°, but we observed a maximum speed at α ~ 60° (Fig. 3B). The mismatch between the experiment and the simulation may be caused by the frictional force between the microswimmer and substrate. At low tilt angle, the streaming flows out from the capsule in all directions and forms a thin liquid layer between the microswimmer and the solid surface (*31*); therefore, the microswimmer can move efficiently with weak acoustic pressure. However, when the tilt angle is large enough to generate a flow on only one side, the microswimmer directly contacts the substrate, and a frictional force is introduced. Both the decrease of the streaming propulsive force in the z direction and the increase of the contact surface between the microswimmer and the solid surface will further increase the frictional force and result in a lower speed. We remark here that these numerical simulations, despite being limited by the lack of an accurate oscillation profile of the water-air interface, provide a good qualitative understanding of the different factors that influence the behavior of the microswimmers.

The dependence of motion on the applied magnetic field provides an additional handle to manipulate the microswimmers, and many useful functions could be developed. For example, by changing the orientation of the Ni layer relative to the capsule axis in the fabrication step, different microswimmers in a mixture could be propelled individually. As shown in Fig. 3D, two types of microswimmers were fabricated by coating the Ni layers in different orientations (deposited at angles of 0° and 20° relative to the long axis of the capsule). When they

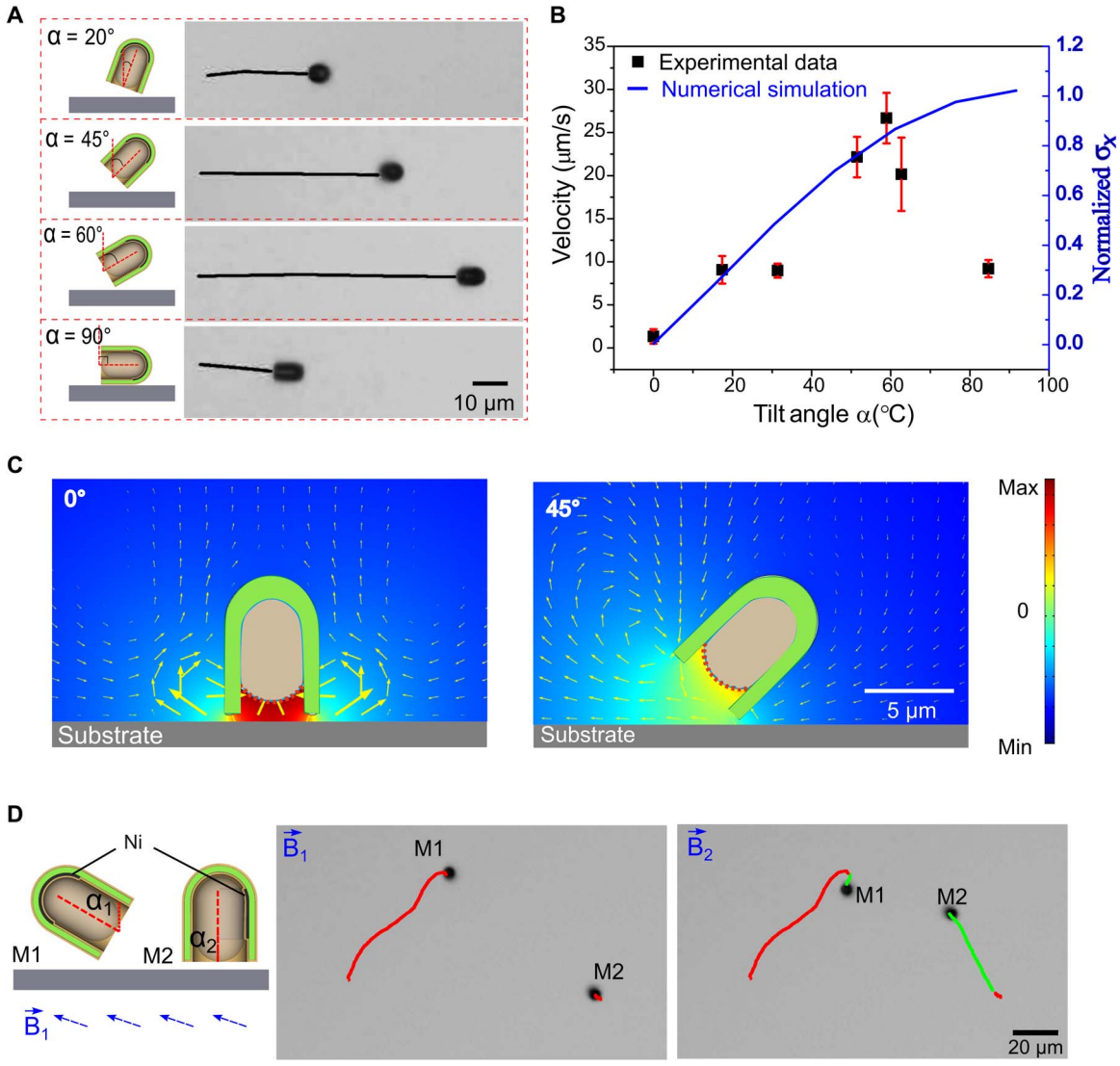

Fig. 3. Regulating the speed of microswimmers by the direction of the magnetic field and numerical simulation of the acoustic streaming pattern. (**A**) An individual microswimmer traveled different distances in 2 s under the same acoustic pressure but with different magnetic field directions. (**B**) Experimental measurement of the microswimmer's speed (black squares) and simulated hydrodynamic stress in the *x* direction σ_x (blue line) when the microswimmer was tilted with different α values. The σ_x is normalized for comparison. (**C**) Numerical simulation of the acoustic pressure (surface) and streaming pattern (arrows) induced by the bubble oscillation at the water-air interface (red dashed lines) when the microswimmer is normal to the substrate (0°) and when it is tilted at α = 45°. A distance of 500 nm was chosen between the substrate and the lowest point of the microswimmer. (**D**) Schematic of microswimmers that were coated with a nickel layer in different orientations and their distinct alignments in the same magnetic field. In a magnetic field B_1 (α_2 = 0), the microswimmer M1 traveled along the red trajectory, while the M2 remained stationary. Then, the magnetic field was rotated (B_2) to make α_1 = 0, the motion of M1 was terminated, and M2 was propelled along the green trajectory.

were mixed and were subjected to the same magnetic field, they aligned in different directions ($\alpha_1 \neq \alpha_2$). If $\alpha_1 \neq 0$, $\alpha_2 = 0$, then the first microswimmer (M1) swam in the chamber, while the second (M2) did not (red trajectories in Fig. 3D). The opposite was achieved by changing the direction of the magnetic field (movie S4). Note that the motions of the two microswimmers are correlated, and this compromises our ability to regulate the speed and direction of the individual microswimmers for selective manipulation.

Particle and cell manipulation

The combination of efficient, precisely directional, and independent propulsion makes the bubble-based microswimmers an ideal tool for selective manipulation of microscopic objects in a crowded group. For demonstration purposes, silica microparticles in water and HeLa cells in cell culture medium were used. Two different manipulation modes (pushing and pulling) were explored. The pushing mode (Fig. 4A) operates at low acoustic pressure, at which the microswimmers exhibit negligible attractive forces on the particles around them. In this situation, the microswimmer loads and transports target particles by moving toward their centers of mass and transmitting its propulsive force to them. The target particles can be easily released by directing the microswimmer away from them. An experimental demonstration is shown in Fig. 4A and movie S5, in which a microswimmer was propelled among a collection of 4-μm-diameter silica particles by a

300-Pa acoustic pressure field and was steered to push only the target particle (highlighted by blue dots). The microswimmer separated the target from an adjacent particle (green dots) with subtle influence on the adjacent particle (the positional shift of the green particle was less than 10 μm), indicating fine control over individual particle manipulation in a crowded group. The pushing mode could work over a broad particle size range and with many types of particles, provided that the propulsive force was strong enough. However, because the pushing force has to pass through the center of mass of the target particle for loading, the pushing mode requires dynamical corrections to the direction of the microswimmer for long-distance transport.

In contrast, an attractive force between the microswimmer and particles could become notable at higher acoustic pressure. This attraction appears to result from a secondary acoustic radiation force that acts on particles that are near the oscillating bubble (*35*, *36*) or near the solid structure of the microswimmer. The attractive force scaled approximately as the square of acoustic pressure and could overcome the drag force on tracer particles to move them along with the microswimmer, as

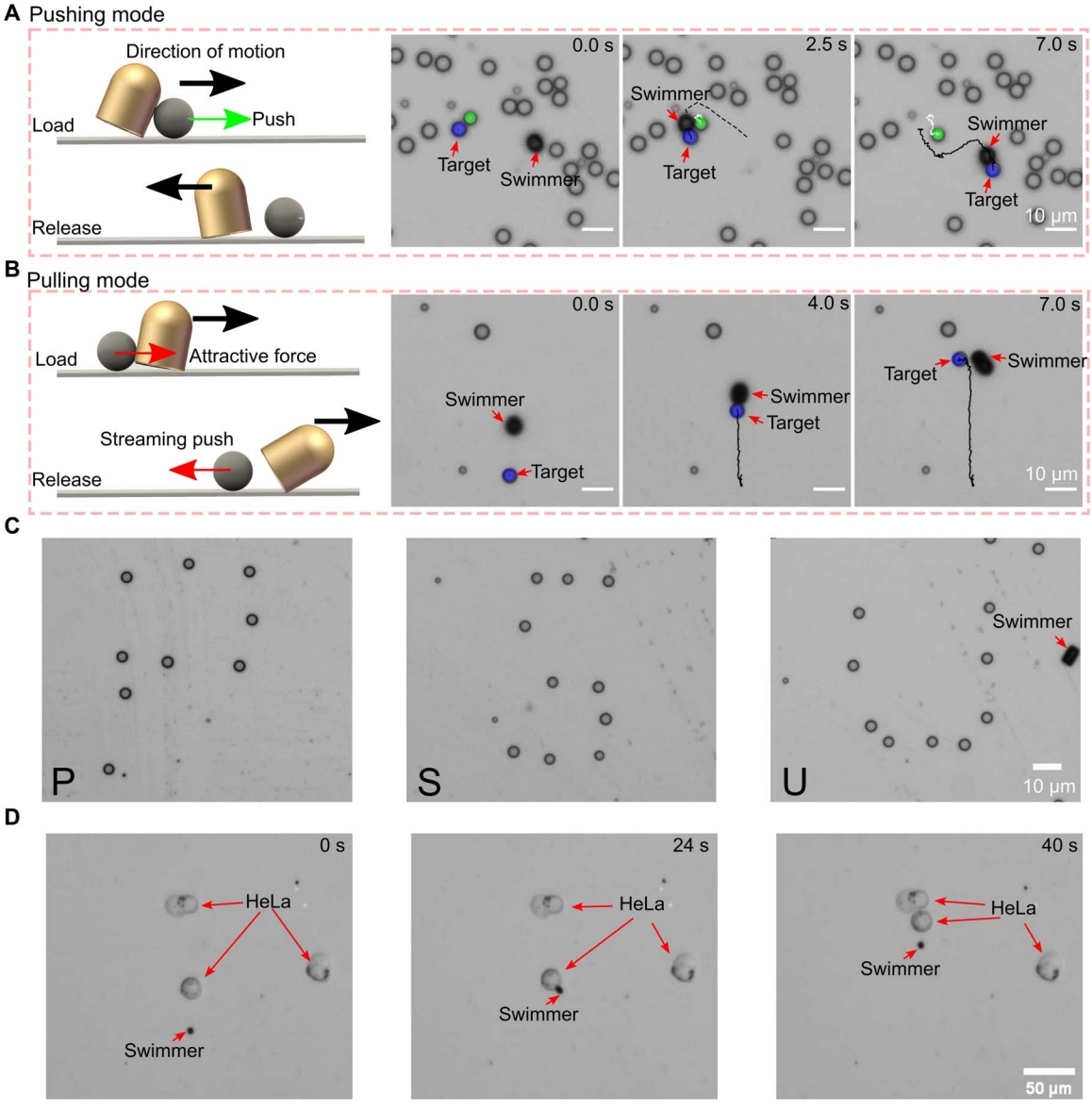

Fig. 4. Manipulation of passive particles with a microswimmer in pushing and pulling modes. (**A**) Illustration of the pushing mode for particle manipulation. Black arrows indicate the motion direction of the microswimmer, and the green arrow indicates the direction of the pushing force. The experimental demonstration was conducted at a low acoustic pressure of 300 Pa. A microswimmer was steered to separate two adjacent particles and push the target particle (blue) away. The weak attractive force between the microswimmer and particles generated a very subtle effect on the green particle. (**B**) Illustration of the pulling mode of the microswimmer for particle manipulation. The black arrows indicate the direction of motion of the microswimmer, and the red arrows indicate the pulling force for loading and the streaming repulsive force for release. This experimental demonstration was conducted at an acoustic pressure of 1 kPa. The microswimmer moved to the target, attracted it, and dragged it to a new location. The particle was released by further tilting the microswimmer to increase the streaming propulsive force on the particle. (**C**) Silica particles (4 μm) were patterned into the letters PSU. (**D**) The microswimmer was propelled in a cell culture medium and pushed a HeLa cell (~20 μm in diameter) into contact with another cell.

illustrated in Fig. 4B. Upon arrival at their new location, the target particle(s) could be released by further tilting the microswimmer to increase the repulsive streaming between them. Particle transport by this pulling mode was experimentally demonstrated at an acoustic pressure of 1 kPa (movie S6). The pulling mode relaxes the requirement for dynamically correcting the direction of the microswimmer and can simultaneously transport multiple particles. However, it depends on strong attractive forces between particles and the microswimmers, which compromises the ability to manipulate individual target particles in crowded situations and limits the scope of use in terms of particle size and materials (*36*). For particles that could be manipulated in either mode, the transition between the two modes depends on the acoustic pressure. Multiple experiments showed that the acoustic field was not strong enough to create significant bulk streaming or pressure nodes to trap passive particles in either the pushing or pulling mode. Thus, multiple particles could be patterned into arbitrary shapes. For example, we patterned silica particles into the letter "P" using the pushing mode and letters "S" and "U" using the pulling mode, producing a "PSU" pattern, as illustrated in Fig. 4C and movie S7. It is a big step forward for acoustic manipulation techniques that our device can move individual passive particles in a high concentration sample and dynamically pattern them into an arbitrary shape.

To validate its potential utility in bioanalytical applications, we used a microswimmer to move cells significantly larger than the microswimmer in a culture medium. Figure 4D shows a free-standing HeLa cell (~20 μm in diameter) transported by the microswimmer to contact another cell in a cell culture medium. Because of the size difference between the cell and the microswimmer, the microswimmer is also able to rotate the cells by generating a torque in the pushing mode. The biocompatibility of the manipulation method was validated by using a two-color cell viability assay (details in Materials and Methods). HeLa cells in Dulbecco's phosphate-buffered saline (DPBS) were stained with calcein-acetoxymethyl (AM) (green fluorescent dye) and ethidium homodimer-1 (red fluorescent dye) and were transferred to the acoustofluidic chamber. As shown in fig. S6, the cells preserved their green fluorescent intensity and did not show red fluorescence or leakage of green fluorescence within 1 hour of manipulation by the microswimmer. The results indicate that neither the acoustic field nor the microswimmers compromise the integrity of the plasma membrane or the intracellular esterase activity.

3D motion along surfaces and in free space

In addition to transporting passive objects, the microswimmers demonstrated a boundary climbing behavior, which allows them to move in complex 3D environments rather than simply on a flat surface. Because of their low density, the gravitational force on the microswimmers is nearly balanced by the buoyancy force. Therefore, the motility of the microswimmers is maintained regardless of the orientation of the substrate. When a microswimmer moves close to a vertical boundary, it experiences attractive forces (F_{SB}) from both the horizontal substrate and the vertical boundary. The open end of the microswimmer rapidly rotates to face the vertical boundary, and its attraction to the latter then dominates its motion, transferring the microswimmer to the vertical boundary. Figure 5A illustrates the orientation of a microswimmer

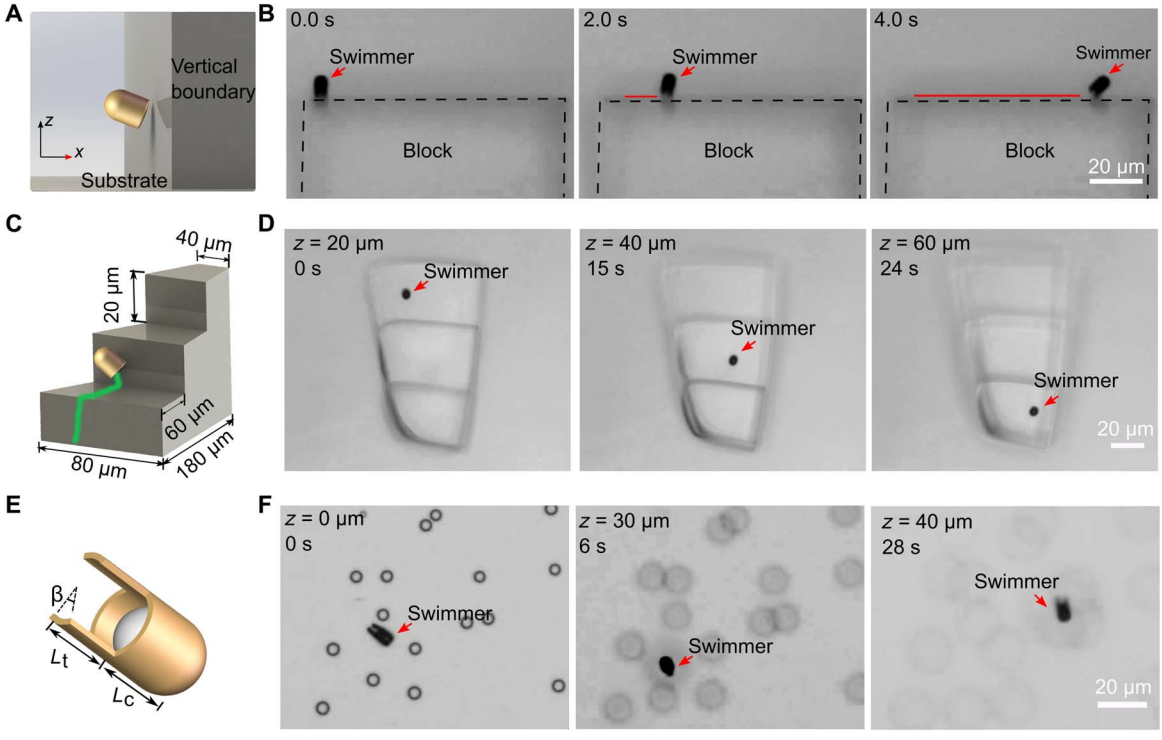

Fig. 5. Manipulation of a microswimmer in 3D. (**A**) Schematic drawing of the orientation of a microswimmer when it is attracted to a vertical boundary. (**B**) A microswimmer moving on a vertical boundary. The microswimmer is initially oriented by acoustic force at the vertical boundary with its open end facing the boundary. The red line shows its trajectory when it was tilted to the right by a magnetic field. (**C**) Schematic of the staircase used to illustrate boundary climbing behavior. The length of each step gradually decreases as their height increases. (**D**) Time-lapse images show the microswimmer climbing the stairs from bottom to top. (**E**) Schematic of a tailed microswimmer. (**F**) Time-lapse images show that a tailed microswimmer detaches from the bottom surface of the cell and moves in free space under magnetic field control.

on a vertical boundary, as demonstrated experimentally in Fig. 5B. The microswimmer had its open end facing the vertical boundary (black dashed lines) and moved toward the right as it was tilted in the same direction. The boundary is a cubic block (edge length, 60 μm) that was printed by direct laser writing. Motion in the vertical direction on this boundary is difficult to track because of the short depth of the focal plane. Here, we fabricated a staircase by the same method to demonstrate the transition of the microswimmer from the horizontal plane to the vertical plane and its vertical motion. The staircase (Fig. 5C) includes three steps, and the height at each step increases by 20 μm. To distinguish the steps, the width of each step decreases gradually as the height increases. As shown in Fig. 5D, a microswimmer climbed the steps and was imaged each time when it reached a new level. A reverse process that drove the microswimmer to a lower step from a higher step was also demonstrated (movie S8). This ability to move over obstacles in 3D significantly enhances the microswimmer's capability for practical applications.

Controllable free swimming in 3D is also a desirable functionality that has not previously been demonstrated for acoustic microswimmers. With simple capsule-shaped swimmers, the motion is confined to solid boundaries due to the strong secondary Bjerknes force. One strategy for suppressing this attraction is to increase the distance between the boundary and the bubble. This was achieved by engineering the microswimmer shape shown in Fig. 5E and fig. S7. Two tails were symmetrically added to the capsule structure. Each of them had an arc angle β of 40° and a length L_t of 4 μm (the length of the capsule L_c is 4 μm). The narrow tails could not support an air bubble between them in water, leading to a water-air interface inside the capsule. When the acoustic field was applied, the attractive force could not rotate the tailed microswimmer due to its extended body, so the streaming propulsive force propelled its translational motion immediately in the absence of a magnetic field. These tailed microswimmers moved autonomously along the bottom surface of the chamber. When they were aligned vertically by a magnetic field, the tails kept the water-air interface away from the boundary and thus lowered the attractive force. In this manner, the streaming propulsive force was able to overcome the attractive force and detach the microswimmer from the substrate. Once in the bulk fluid, the microswimmer could be steered to swim in arbitrary directions in 3D. Figure 5F demonstrates the process of detachment and free swimming in the bulk fluid (movie S9). The change in the *z* position was observed through the defocusing of tracer particles at the bottom of the chamber.

DISCUSSION

We have demonstrated an acoustic bubble-based microswimmer platform with significantly enriched and improved functionality. Several important differences distinguish the behavior of these microswimmers from previously reported, larger acoustic bubble motors. The microcapsule design results in a dominant acoustic secondary Bjerknes force and a strong streaming propulsive force. The microswimmer automatically balances these two forces and requires an external magnetic field to break the balance, leading to precisely directional motion and speed control. As a strong attractive force, the secondary Bjerknes force confines the motion of a microswimmer to the surface of a nearby boundary regardless of the orientation of the boundary. Therefore, the microswimmer can climb vertical boundaries and move through 3D obstacles. The attractive force can also be suppressed by modifying the structure to enable 2D autonomous motion and 3D swimming. The strong streaming propulsive force effectively propels the microswimmers at an acoustic pressure level that has a negligible effect on passive particles in the sample volume, making the microswimmer an ideal tool for microparticle tweezing. Passive particles and cells that are much larger than the microswimmer can thus be patterned into arbitrary shapes using both the pushing and pulling modes.

Here, particle tweezing has been demonstrated only on the bottom surface. Modification of the microswimmer structure, e.g., using a grasper design (*13*), should enable the transport and release of large passive particles in 3D. The precision of microswimmer movement and passive particle tweezing demonstrated here is limited by the manual control of the magnetic field. With the programmable 3D magnetic fields that are widely used with magnetic micromotors (*37*), more precise and sophisticated individual and collective behaviors can be anticipated. To improve their performance in biological applications, the microswimmers could be fabricated from biodegradable polymers and the Ni layer could be replaced by less toxic magnetic materials such as iron oxide nanoparticles. The surface of the microswimmers could be modified or functionalized to minimize their adhesion to tissues (*37*) or for specific target loading. Recently, increasing attention has been focused on the development of intelligent microrobots with hybrid power sources (*38*, *39*). The contactless and biocompatible nature of both the acoustic and magnetic fields make them attractive candidates for these hybrid applications.

In summary, the bubble-based acoustic microswimmers reported here exhibit useful functionality, including 3D controllable motion and precise particle manipulation and patterning in crowded environments, which have not been achieved with other designs. With further experimental investigations, structural modification, and theoretical development, this versatile platform could enable a wide range of applications in micro/nanorobotics.

MATERIALS AND METHODS

Fabrication of the bubble-based microswimmers

Microcapsules were fabricated by 3D Direct Laser Lithography (Nanoscribe GmbH, Germany) using the high-resolution photoresist IP-Dip. Ten thousand capsules could be produced on a fused silica substrate in 4 hours. A Ni layer (thickness of 10 nm) was then deposited onto the top inner surface of the capsules by vertical electron beam deposition (Kurt J. Lesker Lab-18, USA). Ni was alternatively deposited onto the sidewall of the capsules by deposition at an incident angle of 20°. A gold layer (thickness of 40 nm) was then coated over the capsule surface by sputtering (Kurt J. Lesker CMS-18 sputter, USA). To successfully trap air bubbles in the capsules, the samples were incubated in trichloro(1H,1H,2H,2H-perfluorooctyl) silane vapor at 70°C for 15 min to form a hydrophobic monolayer. The samples were cleaned for 20 min by an ultraviolet cleaner (PSD-UVT, USA) before the surface treatment. Last, the completed capsules were scratched off the substrate by means of a pipette tip and were transferred to a fluidic chamber.

Experimental setup

The fluidic chamber was fabricated by attaching multiple layers of ring-shaped polyimide Kapton tape (5 mm in inner diameter, thickness of 60 μm) onto a single-side polished silicon wafer (thickness of 500 μm). A microscope coverslip (thickness of 100 μm) was used to cover the cylindrical chamber after filling it with solution. The height of the chamber was adjusted by changing the number of Kapton tape layers. A piezo ceramic transducer (10 MHz; STEMiNC Inc.) was glued to the

opposite side of the silicon wafer using Aquasonic 100 Ultrasound Transmission Gel and was fixed by a clamp. This 10-MHz transducer was chosen to ensure a uniform acoustic pressure output in the frequency range of 1 to 3 MHz (fig. S8). The magnetic field was generated by using a cylindrical magnet (DEE, K&J Magnetics Inc., USA), which was placed under the chamber. The distance between the magnet and the chamber was about 10 cm. The thin nickel layer in the microswimmer aligned perpendicular to the axial direction of the magnet in this magnetic field.

Experiments were conducted with an Olympus BX60 light microscope. Images and videos were captured by a USB camera (Flea3, Flir Integrated Imaging Solutions Inc., Canada) mounted on the microscope and were analyzed by using open-source software, ImageJ (National Institutes of Health, USA). The acoustic transducer was driven by an radio frequency (RF) signal function generator (33120A, Agilent, USA). The acoustic pressure in the fluidic chamber was characterized using a hydrophone (HGL-0085, Onda Inc., USA) at a distance of ~13 mm from the surface of the silicon wafer and calculated on the basis of an attenuation coefficient of 0.00015 Neper/cm.

Numerical simulations

The numerical simulations in Fig. 3C were conducted using COMSOL Multiphysics finite element software. This model was validated by comparing the streaming pattern from the simulation with that from the experiment of a microswimmer fixed parallel to the bottom (fig. S9). The streaming phenomenon was simulated by considering a perturbation expansion approach wherein the flow variables were separated into their first- and second-order components (*40*). The first-order components, which are indicative of the acoustic response of the system, were considered to be harmonically oscillating (with a frequency equal to the actuation frequency). In contrast, the second-order components represent the time-averaged response of the system, evolving on a much slower time scale than the acoustic wave period. This separation of variables results in the reduction of Navier-Stokes equations into two separate systems of equations for the first- and second-order components of the flow variables. These systems of equations were solved in a sequential manner wherein the first-order system of equations was solved using a frequency-domain approach, while steady-state solutions were sought for the time-averaged, second-order system of equations. We performed a 2D simulation on a rectangular domain with a length of 100 μm and a width of 140 μm. We used impedance boundary conditions at all boundaries, except the water-air interface. The acoustic actuation was modeled using a Dirichlet boundary condition at the water-air interface, which was assumed to be oscillating at the actuation frequency in the radial direction. An unstructured triangular mesh with 7975 elements was used. We used P1-P2 composite elements for the pressure and velocity, where P1 and P2 denote the triangular elements with Lagrange polynomials of orders 1 and 2, respectively. For both the first- and second-order systems of equations, a direct solver was used to obtain the solution.

Cell and particle preparation

HeLa cells (CCL-2, American Type Culture Collection, USA) were cultured using cell culture media (Eagle's minimum essential medium modified with 10% fetal bovine serum) in a 37°C cell culture incubator. Before the experiment, the cultured cells were suspended in the same culture media and transferred to the acoustic fluidic chamber with a pipette. The experiments were conducted immediately after the transfer to prevent adhesion of cells to the substrate. Silica beads (Sigma-Aldrich, USA) and polystyrene beads (Bangs Laboratories Inc., USA) were diluted with deionized water to appropriate concentrations for particle patterning and streaming tracking purposes.

Cell viability testing

Cell viability was tested by using a two-color dual-parameter cell viability assay (Thermo Fisher Scientific, USA). HeLa cells (~10^5/ml) were suspended in DPBS with 1.2 μM ethidium homodimer-1 and 3.6 μM calcein-AM. After incubation for 30 min at room temperature, the cells were mixed with microswimmers and transferred to the acoustofluidic chamber for manipulation. An acoustic field with a pressure level of 1 kPa was applied to actuate the microswimmers, and the process of transporting cells with the microswimmers was continued for 5 to 10 min. The intensities of the green fluorescence and red fluorescence of the cells were recorded every 10 min for 1 hour after the cells were manipulated. Ten cells were analyzed in fig. S6B and in a control group of cells without the acoustic treatment.

SUPPLEMENTARY MATERIALS

Supplementary material for this article is available at http://advances.sciencemag.org/cgi/content/full/5/10/eaax3084/DC1

Fig. S1. Fabrication process of microswimmers.
Fig. S2. Optical microscopic image of an uncoated microswimmer floating in water.
Fig. S3. Experimental distribution of the resonant frequency of microswimmers and theoretical calculation.
Fig. S4. Characterization of the resonant frequencies of a small microswimmer (a = 1 μm).
Fig. S5. Schematic of the response of an uncoated microswimmer in the fluidic chamber.
Fig. S6. HeLa cell viability assay.
Fig. S7. Scanning electron microscopy image of tailed microswimmers.
Fig. S8. Measurement of the acoustic pressure with a hydrophone at a distance of ~13 mm from the surface of the silicon wafer, the input voltage was 10 Vpp.
Fig. S9. Simulated and experimental streaming patterns.
Movie S1. The self-rotation of a microswimmer responding to an acoustic field.
Movie S2. The magnetic field–initiated steerable translational motion of a microswimmer.
Movie S3. An individual microswimmer traveled different distances in 2 s under the same acoustic pressure but with different tilt angles.
Movie S4. Two microswimmers were propelled independently in the mixture by changing the direction of a magnetic field.
Movie S5. Separation of two adjacent silica particles with the microswimmer in its pushing mode.
Movie S6. Transport of particles with the microswimmer in its pulling mode.
Movie S7. Patterning particles in the shapes of letters PSU by a microswimmer.
Movie S8. A microswimmer climbing up and down a stairway.
Movie S9. A tailed microswimmer free swimming in 3D.

REFERENCES AND NOTES

1. P. J. Pauzauskie, A. Radenovic, E. Trepagnier, H. Shroff, P. Yang, J. Liphardt, Optical trapping and integration of semiconductor nanowire assemblies in water. *Nat. Mater.* **5**, 97–101 (2006).
2. A.-E. Saliba, A. J. Westermann, S. A. Gorski, J. Vogel, Single-cell RNA-seq: Advances and future challenges. *Nucleic Acids Res.* **42**, 8845–8860 (2014).
3. P. L. Johansen, F. Fenaroli, L. Evensen, G. Griffiths, G. Koster, Optical micromanipulation of nanoparticles and cells inside living zebrafish. *Nat. Commun.* **7**, 10974 (2016).
4. J. P. Desai, A. Pillarisetti, A. D. Brooks, Engineering approaches to biomanipulation. *Annu. Rev. Biomed. Eng.* **9**, 35–53 (2007).
5. A. Ashkin, Optical trapping and manipulation of neutral particles using lasers. *Opt. Photonics News* **10**, 41 (1999).
6. I. De Vlaminck, C. Dekker, Recent advances in magnetic tweezers. *Annu. Rev. Biophys.* **41**, 453–472 (2012).
7. A. Ozcelik, J. Rufo, F. Guo, Y. Gu, P. Li, J. Lata, T. J. Huang, Acoustic tweezers for the life sciences. *Nat. Methods* **15**, 1021–1028 (2018).
8. W. Wang, W. Duan, S. Ahmed, T. E. Mallouk, A. Sen, Small power: Autonomous nano- and micromotors propelled by self-generated gradients. *Nano Today* **8**, 531–554 (2013).

9. Y. Tu, F. Peng, D. A. Wilson, Motion Manipulation of Micro- and Nanomotors. *Adv. Mater.* **29**, 1701970 (2017).
10. K. Kim, J. Guo, Z. Liang, D. Fan, Artificial Micro/Nanomachines for bioapplications: Biochemical delivery and diagnostic sensing. *Adv. Funct. Mater.* **28**, 1705867 (2018).
11. M. Luo, Y. Feng, T. Wang, J. Guan, Micro-/Nanorobots at work in active drug delivery. *Adv. Funct. Mater.* **28**, 1706100 (2018).
12. J. Li, B. Esteban-Fernández de Ávila, W. Gao, L. Zhang, J. Wang, Micro/nanorobots for biomedicine: Delivery, surgery, sensing, and detoxification. *Sci. Robot.* **2**, eaam6431 (2017).
13. S. Tottori, L. Zhang, F. Qiu, K. K. Krawczyk, A. Franco-Obregón, B. J. Nelson, Magnetic helical micromachines: Fabrication, controlled swimming, and cargo transport. *Adv. Mater.* **24**, 811–816 (2012).
14. D. Schamel, A. G. Mark, J. G. Gibbs, C. Miksch, K. I. Morozov, A. M. Leshansky, P. Fischer, Nanopropellers and their actuation in complex viscoelastic media. *ACS Nano* **8**, 8794–8801 (2014).
15. E. B. Steager, M. Selman Sakar, C. Magee, M. Kennedy, A. Cowley, V. Kumar, Automated biomanipulation of single cells using magnetic microrobots. *Int. J. Rob. Res.* **32**, 346–359 (2013).
16. T. Xu, L. P. Xu, X. Zhang, Ultrasound propulsion of micro-/nanomotors. *Appl. Mater. Today* **9**, 493–503 (2017).
17. K. J. Rao, F. Li, L. Meng, H. Zheng, F. Cai, W. Wang, A force to be reckoned with: A review of synthetic microswimmers powered by ultrasound. *Small* **11**, 2836–2846 (2015).
18. W. Wang, L. A. Castro, M. Hoyos, T. E. Mallouk, Autonomous motion of metallic microrods propelled by ultrasound. *ACS Nano* **6**, 6122–6132 (2012).
19. M. Kaynak, A. Ozcelik, A. Nourhani, P. E. Lammert, V. H. Crespi, T. J. Huang, Acoustic actuation of bioinspired microswimmers. *Lab Chip* **17**, 395–400 (2017).
20. D. Ahmed, T. Baasch, B. Jang, S. Pane, J. Dual, B. J. Nelson, Artificial swimmers propelled by acoustically activated flagella. *Nano Lett.* **16**, 4968–4974 (2016).
21. D. Ahmed, M. Lu, A. Nourhani, P. E. Lammert, Z. Stratton, H. S. Muddana, V. H. Crespi, T. J. Huang, Selectively manipulable acoustic-powered microswimmers. *Sci. Rep.* **5**, 9744 (2015).
22. R. J. Dijkink, J. P. van der Dennen, C. D. Ohl, A. Prosperetti, The 'acoustic scallop': A bubble-powered actuator. *J. Micromech. Microeng.* **16**, 1653–1659 (2006).
23. J. Feng, J. Yuan, S. K. Cho, Micropropulsion by an acoustic bubble for navigating microfluidic spaces. *Lab Chip* **15**, 1554–1562 (2015).
24. D. Ahmed, C. Dillinger, A. Hong, B. J. Nelson, Artificial acousto-magnetic soft microswimmers. *Adv. Mater. Technol.* **2**, 1700050 (2017).
25. T. Qiu, S. Palagi, A. G. Mark, K. Melde, F. Adams, P. Fischer, Wireless actuation with functional acoustic surfaces. *Appl. Phys. Lett.* **109**, 191602 (2016).
26. T. Qiu, S. Palagi, A. G. Mark, K. Melde, F. Adams, P. Fischer, Active acoustic surfaces enable the propulsion of a wireless robot. *Adv. Mater. Interfaces* **4**, 1700933 (2017).
27. L. Ren, D. Zhou, Z. Mao, P. Xu, T. J. Huang, T. E. Mallouk, Rheotaxis of bimetallic micromotors driven by chemical-acoustic hybrid power. *ACS Nano* **11**, 10591–10598 (2017).
28. S. Ahmed, W. Wang, L. O. Mair, R. D. Fraleigh, S. Li, L. A. Castro, M. Hoyos, T. J. Huang, T. E. Mallouk, Steering acoustically propelled nanowire motors toward cells in a biologically compatible environment using magnetic fields. *Langmuir* **29**, 16113–16118 (2013).
29. V. Garcia-Gradilla, J. Orozco, S. Sattayasamitsathit, F. Soto, F. Kuralay, A. Pourazary, A. Katzenberg, W. Gao, Y. Shen, J. Wang, Functionalized ultrasound-propelled magnetically guided nanomotors: Toward practical biomedical applications. *ACS Nano* **7**, 9232–9240 (2013).
30. N. Bertin, T. A. Spelman, O. Stephan, L. Gredy, M. Bouriau, E. Lauga, P. Marmottant, Propulsion of bubble-based acoustic microswimmers. *Phys. Rev. Appl.* **4**, 064012 (2015).
31. J.-F. Louf, N. Bertin, B. Dollet, O. Stephan, P. Marmottant, Hovering microswimmers exhibit ultrafast motion to navigate under acoustic forces. *Adv. Mater. Interfaces* **5**, 1800425 (2018).
32. T. G. Leighton, *The Acoustic Bubble* (Elsevier, 1994); https://linkinghub.elsevier.com/retrieve/pii/B9780124419209X50019.
33. B. Dollet, P. Marmottant, V. Garbin, Bubble dynamics in soft and biological matter. *Annu. Rev. Fluid Mech.* **51**, 331–355 (2019).
34. T. A. Spelman, thesis, University of Cambridge (2017).
35. D. L. Miller, Particle gathering and microstreaming near ultrasonically activated gas-filled micropores. *J. Acoust. Soc. Am.* **84**, 1378–1387 (1988).
36. P. Rogers, A. Neild, Selective particle trapping using an oscillating microbubble. *Lab Chip* **11**, 3710–3715 (2011).
37. Z. Wu, J. Troll, H.-H. Jeong, Q. Wei, M. Stang, F. Ziemssen, Z. Wang, M. Dong, S. Schnichels, T. Qiu, P. Fischer, A swarm of slippery micropropellers penetrates the vitreous body of the eye. *Sci. Adv.* **4**, eaat4388 (2018).
38. C. Chen, F. Soto, E. Karshalev, J. Li, J. Wang, Hybrid nanovehicles: One machine, two engines. *Adv. Funct. Mater.* **29**, 1806290 (2018).
39. L. Ren, W. Wang, T. E. Mallouk, Two forces are better than one: Combining chemical and acoustic propulsion for enhanced micromotor functionality. *Acc. Chem. Res.* **51**, 1948–1956 (2018).
40. N. Nama, R. Barnkob, Z. Mao, C. J. Kähler, F. Costanzo, T. J. Huang, Numerical study of acoustophoretic motion of particles in a PDMS microchannel driven by surface acoustic waves. *Lab Chip* **15**, 2700–2709 (2015).

Acknowledgments: We thank A. Dangi and C. Cheng for their help with acoustic pressure measurements. We thank the Shorter Lab and H. Odeh for providing HeLa cells for the cell viability assays. Part of this work was carried out in the Nanofabrication Laboratory at Penn State's Materials Research Institute. **Funding:** This work was supported by the National Science Foundation under MRSEC grant number DMR-1420620. F.S. acknowledges a fellowship from the UC MEXUS-CONACYT. **Author contributions:** T.E.M., L.R., and J.W. conceived the project, and T.E.M., W.W., and J.W. supervised the research. L.R., W.W., and F.S. designed the experiments. L.R. and J.M.M. fabricated the samples, conducted the experiments, and processed the data. L.R. and N.N. conducted numerical simulations and theoretical analyses. J.M.M. and W.L. conducted the cell viability assays. Z.Y. performed the metallic layer deposition. T.E.M., L.R., and W.W. wrote the manuscript, and all the authors contributed to the final version. **Competing interests:** The authors declare that they have no competing interests. **Data and materials availability:** All data needed to evaluate the conclusions in the paper are present in the paper and/or the Supplementary Materials. Additional data related to this paper may be requested from the authors.

Submitted 12 March 2019
Accepted 13 September 2019
Published 25 October 2019
10.1126/sciadv.aax3084

Citation: L. Ren, N. Nama, J. M. McNeill, F. Soto, Z. Yan, W. Liu, W. Wang, J. Wang, T. E. Mallouk, 3D steerable, acoustically powered microswimmers for single-particle manipulation. *Sci. Adv.* **5**, eaax3084 (2019).

Science Advances

3D steerable, acoustically powered microswimmers for single-particle manipulation

Liqiang Ren, Nitesh Nama, Jeffrey M. McNeill, Fernando Soto, Zhifei Yan, Wu Liu, Wei Wang, Joseph Wang and Thomas E. Mallouk

Sci Adv **5** (10), eaax3084.
DOI: 10.1126/sciadv.aax3084